Microcoil MRI of plants and algae at ultra-high field : an exploration of metabolic imaging

Schadewijk, R. van

4 MR MICROSCOPY OF *MEDICAGO TRUNCATULA* AT 22.3 TESLA

Cellular Resolution and Localised Spectroscopy

4.1 ABSTRACT

Interactions between plants and the soil's microbial & fungal flora are crucial for the health of soil ecosystems and food production. Microbe-plant interactions are difficult to investigate *in situ* due to their intertwined relationship involving morphology and metabolism. Here, an approach is described to overcome this challenge by elucidating morphology and the metabolic profile of *Medicago truncatula* root nodules using Magnetic Resonance (MR) Microscopy, at the highest magnetic field strength (22.3 T) currently available for imaging. A home-built solenoid MR signal detector with an inner diameter of 1.5 mm was used to study individual root nodules. A 3D imaging sequence with an isotropic resolution of $(7\ \mu m)^3$ was able to resolve individual cells, and distinguish between cells infected with rhizobia and uninfected cells. Furthermore, the metabolic profile of cells in different sections of the root nodule was studied using localised MR spectroscopy, showing that several metabolites, including betaine, asparagine/aspartate and choline, vary across nodule zones. The metabolite spatial distribution was visualised using chemical shift imaging. Finally, the technical challenges and outlook towards future *in vivo* MR microscopy of nodules and the plant root system are described.

This chapter is based on:

van Schadewijk, R., Krug, J.R., Shen, D., Sankar Gupta, K.B.S., Vergeldt, F.J., Bisseling, T., Webb, A., Van As, H., Velders, A.H., de Groot H.J.M., Alia, A. (2020) Magnetic Resonance Microscopy at Cellular resolution and Localised Spectroscopy of *Medicago truncatula* at 22.3 T. *Sci Rep* **10,** 971. https://doi.org/10.1038/s41598-020-57861-7

4.2 INTRODUCTION

Interactions between plants and microbes are considered to be crucial for the health of the soil ecosystem as a whole (Doran and Zeiss, 2000). Understanding the metabolic interactions between plants and microbes, both commensal and parasitic, could help address many of the challenges we face today, related to agriculture and food security. One such interaction is the microbiome-mediated uptake of nitrogen by plants. Availability of biologically-active forms of nitrogen in the soil is one of the most crucial factors determining crop yield. Current agricultural practice, therefore, relies strongly on nitrogen fertiliser to supplement soil nitrogen to ensure high crop yield (Smil, 2001). The Haber-Bosch nitrogen fixation process, used to produce the ammonia needed for these fertilisers, currently consumes 1% of the world energy sources; making it the most energy consuming process in the chemical industry (Smith, 2002). In contrast, alternative processes (*e.g.* symbiotic nitrogen fixation, SNF) achieve the same result of fixing nitrogen without the need for high pressure and temperature required by the Haber-Bosch process.

More precisely, plants have solved the problem of biological nitrogen fixation through commensal processes, involving bacterial infection of plant roots (Suzaki, Yoro and Kawaguchi, 2015). Mutualistic infections are omnipresent in nature, with a wide range of nitrogen-fixing bacteria – such as those that are collectively named rhizobium – invading not just plants but also the phycosphere of green algae (Kim *et al.*, 2014). The mutualistic symbiosis involves almost all parts of the plant cell machinery, including plastids and mitochondria. Of particular interest are the interactions between rhizobial bacteria and leguminous plants, which form dedicated organs - root nodules - to accommodate the bacteria. *Medicago. truncatula* infected with *Sinorhizobium meliloti* (*S. meliloti*) has long since been used as a model plant system to study plant-rhizobia interactions (Barker *et al.*, 1990). The root nodules facilitate intracellular hosting and nutrient exchange(Nap and Bisseling, 1990). The result is the efficient formation of fixed nitrogen (NH_4^+), which provides considerable growth advantages to leguminous plants (Udvardi and Day, 1997). Recently, a detailed fate map of root nodule formation at a genetic level has been developed (Xiao *et al.*, 2014). It has also been proposed that rhizobial metabolic activity may confer resistance to drought and salt stress (López, Tejera and Lluch, 2009; Kunert *et al.*, 2016; Staudinger *et al.*, 2016). More detailed understanding of key metabolites in plant-nodule metabolism and importantly, their localisation within root nodule tissues could, therefore, shed light on the mechanism by which Symbiotic Nitrogen Fixation (SNF) confers advantages to host plants.

Tracking metabolite exchange non-invasively within intact nodule systems is difficult with most imaging modalities, since they require a form of sample fixation, for example in the case of Matrix Assisted Laser Desorption/Ionisation Mass Spectrometry (MALDI-MS) imaging (Ye *et al.*, 2013). The current knowledge of the metabolic profile in the root nodules is based on analysis with destructive extraction procedures. For example, Gas Chromatography and Liquid Chromatography in combination with Mass Spectrometry

(GC/LC-MS) has provided rich metabolic information but required destructive extraction procedures (Ogden *et al.*, 2017). These *in vitro* methods may not faithfully reflect the native structural and molecular information. Examining and mapping the levels of metabolites directly in the intact root nodule, non-invasively, would be important to understand the functional framework of metabolism in the native state. Magnetic resonance techniques may offer advantages in terms of spatially resolved spectroscopic information on a single nodule, which is difficult to access with alternative techniques. Magnetic resonance imaging (MRI) has been previously used to visualize belowground root structures (Metzner *et al.*, 2014; Schmittgen *et al.*, 2015; van Dusschoten *et al.*, 2016). In this chapter, state-of-the-art magnetic resonance microscopy (MRM) is applied in conjunction with localised spectroscopy at ultra-high magnetic field (22.3T), using a home-built solenoid RF coil, in order to image root nodules of *Medicago truncatula*. Not only cellular level structural information is obtained but also a mapping of metabolic information in localised zones, and how they vary across different tissues. Lastly, I describe the technical challenges and outlook towards future *in vivo* imaging of nodules and plant root systems.

4.3 RESULTS

4.3.1 ROOT NODULE MORPHOLOGY RESOLVED BY MR MICROSCOPY IN CELLULAR DETAIL

A representative *M. truncatula* specimen with a single root nodule shown in Fig. 4.1A, was imaged using a custom home-built 1.5 mm diameter solenoid coil as depicted in Fig. 4.1B.

Figure 4.1 Photograph of M. truncatula root system and custom-designed home-built microcoil. (**A**) Photograph of a representative M. truncatula plant (five weeks old, three weeks post inoculation). Typical root nodule indicated with a red square. Some white perlite beads are still visible along the root system. (**B**) Photograph of a home-built solenoid coil insert mounted on a Bruker insert holder. The solenoid inner diameter is 1.5 mm; further details are described in the materials and methods.

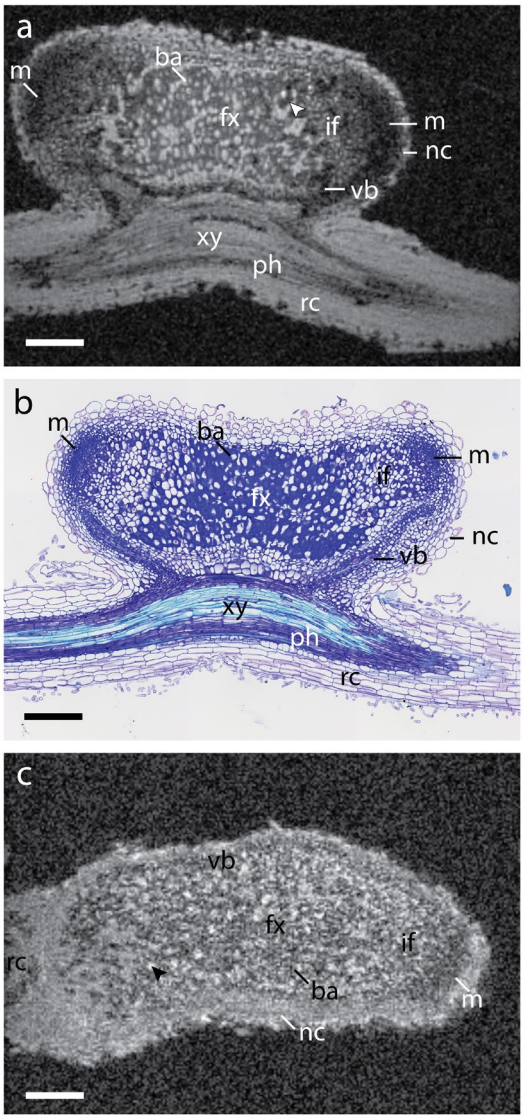

Figure 4.2 High-resolution MR imaging and optical microscopy of root nodules. (**A**) FLASH image of fixed root nodule at 7 × 7 × 7 μm^3 resolution. Individual cells containing bacteroids (ba) can be discerned by the dark rings inside the cells, where *S. meliloti* cells accumulate. The nodule exhibits a double meristem (m) on opposed directions with cells becoming smaller towards the meristem until individual cells can no longer be resolved. Air pockets appear as hypo-intense regions marked with an arrowhead. (**B**) Optical transmission microscopy of nodule section (thickness 5 μm) stained with Toluidine blue. (**C**) FLASH image of *in vivo* root nodule at 7 × 7 × 7 μm^3 resolution. Though lower in signal-to-noise, both uninfected cells (black arrow) and infected cells (ba) can be discerned. Abbreviations: rc, root cortex; xy, xylem; ph, phloem; nc, nodule cortex; vb, vascular bundle; fx, fixation zone; if, infection zone; ba, bacteroid containing cells; m, meristem. Scale bars 200μm.

Individual cells of a root nodule with two lobes and meristems (m) could be distinguished on the MRI scans. A high-resolution 3D Fast Low Angle SHot (FLASH) image of the fixed root nodule is shown in Fig. 4.2A. All image slices through the entire root nodule are shown in the supplementary material (Supplementary Video 4.S1). Root nodule morphology in *M. truncatula* nodules are of the indeterminate type, *i.e.*, four distinct regions (zones) occur, from the apex of the root nodule to the root attachment point (Suzaki, Yoro and Kawaguchi, 2015). Nodule tissue - from outward to inward - starting with the nodule cortex (nc), delineated as a high-intensity ring on the surface of the nodule, contrasted with the darker region of the meristem (m). Cells in the meristem, responsible for the growth of the nodule, were significantly smaller than mature bacteroid containing cells. In the next region, the rhizobial infection zone (if), young cells infected by rhizobia bacteria could be seen as a region of alternating high- and low-intensity patches. Not all cells in the rhizobial infection zone were infected, which was apparent due to the presence of variation in image intensities, *i.e.*, non-infected plant cells had a higher image intensity as compared to cells infected with the bacterium. Lastly, in the active nitrogen fixation zone (fx), large cells (40 to 50 µm) could be distinguished by their grey rings, caused by the presence of bacteroids surrounding the vacuole (Gavrin *et al.*, 2014). The fixation zone is where rhizobia make nitrogenase, the enzyme required for nitrogen fixation. In the same area, uninfected interstitial cells were visible, which did not exhibit the rings. These interstitial cells perform an important role in the regulation of nitrogen fixation activity (Dakora and Atkins, 1991). Lastly, connective tissues (vascular bundles) could be seen extending from the root towards the periphery of the nodules, providing a route for nutrient exchange with the rest of the plant.

Fig. 4.2B shows a light microscopy image of a histological slice stained with Toluidine blue, from the same root nodule at approximately the same plane as the MR image (co-registration). Toluidine blue stained the nuclei and lignin of the cell wall (O'Brien, Feder and McCully, 1964). Common features in Fig. 4.2A and 4.2B are seen, including the bacteroid ring as observed on the MR image, occurring in the staining of cells in the nitrogen fixation zone. Especially visible were the vascular bundles extending from the central root, which due to their smaller cells appeared more densely stained in the optical microscopy image. In addition, air pockets could also be imaged as they appeared as hypo-intense regions in the FLASH image (Fig. 4.2A, arrowhead). Air pockets also introduced differences in magnetic susceptibility within the sample, which influenced image quality. Air pockets of different sizes could be seen within the fixation zone using multiple gradient echo (MGE) imaging with echoes acquired at increasing echo times (Supplementary Fig. 4S2). Because of the abundance of air pockets in the apical zone, the susceptibility-induced hypointense regions also increased in size in the apical direction.

To evaluate the possibilities of high-resolution MR imaging of root nodule without any fixation or treatment, measurements were performed on freshly excised nodules (Fig. 4.2C). While the image contrast and signal-to-noise ratio (SNR) was noticeably reduced,

individual cells in the nitrogen fixation zone could still be distinguished. The uninfected cells appeared bright while infected cells appeared dark in the active infection zone.

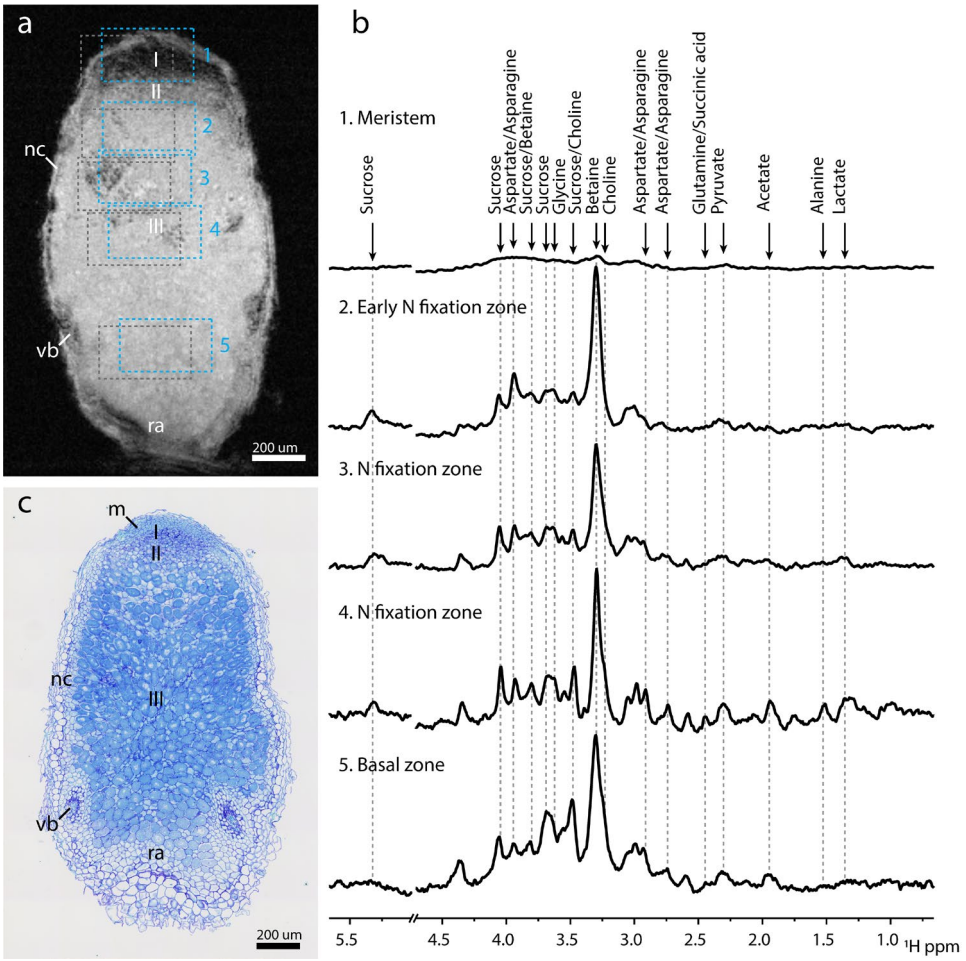

Figure 4.3 Localised spectroscopy in *in-situ* root nodule reveals sugar differences in pre- and post-granule onset regions. (**A**) FLASH reference with PRESS Region of Interest (ROI), numbered one through five. Roman numerals indicate nodule zones: Meristem (I), Infection zone (II), Nitrogen fixation zone (III). Grey dotted boxes show ROI shift of Betaine due to Chemical Shift Displacement Error (CDSE). Pulse excitation was centred around 4.0 ppm. (**B**) Co-registration of Optical Microscopy confirms the presence of bacteroids in the active nitrogen fixation region. Toluidine blue staining 10x magnification. (**c**) PRESS spectra captured from Regions of Interest (ROI) shown in Fig. 3A, for Nodule Meristem (1), (early) Nitrogen fixation zone (2), Nitrogen fixation zone (3 & 4), Basal region (5). PRESS voxel sizes were 200 × 350 × 350 μm^3. Spectra were aligned to the betaine peak at 3.3 ppm. Water peak region at 4.7 ppm has been omitted for ease of viewing. Intensities of the spectra have not been normalised, reflecting the strength of the signal recorded. This means that for the meristem little information can be discerned. Line broadening 10 Hz. Abbreviations: nc, nodule cortex; vb, vascular bundle; m, meristem; ra, root attachment area. Scale bars 200 μm.

4.3.2 MR SPECTROSCOPY REVEALED THE SPATIAL DISTRIBUTION OF NODULE METABOLITES

Since the root nodule is an active plant organ whose primary function is to fix nitrogen and to facilitate nutrient exchange, SNF-linked metabolite distribution over the various nodule zones is of interest. According to earlier literature, a nodule may be divided into four zones, based on SNF activity: (I) meristem zone, (II) infection zone, (III) nitrogen fixation zone, and (IV) senescence zone, the latter observed mostly in older nodules. In the infection zone, bacteroids accumulate and mature, while in the fixation zone active SNF takes place(Dupont *et al.*, 2012). Localised Magnetic Resonance Spectroscopy (MRS) was utilised to distinguish metabolites, based on their frequency differences (chemical shift) and location. Localised MR spectra were recorded from five different regions of interest (ROI), localised in the four different zones in an intact freshly excised root nodule, *in situ* (Fig. 4.3A). The presence of bacteroids was verified with optical microscopy after the MRI measurements (Fig. 4.3C). The first ROI was placed on the meristem (ROI 1) in Fig. 4.3B, where little MR signal was recorded, possibly due to the small volumes of individual cells which may cause T_2-shortening, reducing the SNR. The second voxel (ROI 2) was placed in the infection/early fixation zone. The third (ROI 3) and fourth voxels (ROI 4) were placed in the largest zone: the active nitrogen fixation zone. The last voxel (ROI 5) was placed in the basal region of the root nodule.

The spectra obtained from ROIs 2-5 showed the presence of several metabolites including various amino acids, sugars, choline and betaine. Betaine was present in a high amount in all four ROIs (Fig. 4.3B). The signal from sucrose and asparagine/aspartate was also clearly detected. Assignment of various metabolites was confirmed with solution-state NMR performed on an extract obtained from the root nodules, using two-dimensional ^{1}H-^{1}H correlation spectroscopy (2D-COSY) (see Supplementary Fig. 4.S3). It should be noted that, due to the chemical shift displacement error, which increases with magnetic field strength, the regions of interest chosen for the localised spectra were shifted slightly for each metabolite, as the spatial selection relied on the frequency of the metabolite relative to the chosen centre frequency of 4.0 ppm(van der Graaf, 2010). This shift meant that the indicated regions of interest in Fig. 3a were correct for signals at δ = 4 ppm, while for example the strongest signal (at δ = 3.3 ppm) originated from an ROI which was shifted by 35 µm along x, 97 µm along y and 97 µm along z (see the dotted region of interest in Fig. 4.3A).

The strongest peak observed in all spectra was attributed to a resonance of glycine betaine (δ = 3.3 ppm) (Fig. 4.3B). A complementary spectroscopic imaging method, Chemical shift imaging (CSI) confirmed the presence of betaine throughout the nodule (Supplementary Fig. 4.S4). Betaine serves as an important osmoprotectant produced by *S. meliloti* (Smith *et al.*, 1988). Furthermore choline - a precursor to glycine betaine in both plants and bacteria - was visible in ROI 3 as a shoulder on the low frequency side of the betaine peak, and was even more pronounced in ROIs 4 and 5 (Ashraf and Foolad, 2007). In uninfected root tissue, choline, but not glycine betaine was detected as seen in solution NMR measurements (Supplementary Fig. 4.S5).

In root nodule, another strong peak from asparagine and aspartate was seen primarily in ROIs 2-5 (Fig. 4.3B). Notably, glutamine - though present in ROI 4 - appeared much lower in concentration in all ROIs than asparagine, suggesting a smaller pool or higher turnover rate in the nitrogen assimilation process.

Intermediates from the tricarboxylic acid cycle such as acetate (δ = 1.9 ppm), pyruvate (δ = 2.3 ppm) and succinic acid (δ = 2.4 ppm) were also seen in the nitrogen fixation zone (region 3 & 4). Lactate (δ = 1.3 ppm) was visible only in the active nitrogen fixation zone (region 3 & 4). Alanine (δ = 1.5 ppm) has been suggested by metabolic network modelling to be the primary metabolite for the uptake of assimilated nitrogen by plants (Pfau *et al.*, 2016). However, our results indicated that the pool of alanine was small compared to asparagine.

Sucrose, the most important resource for growth and root nodule activity, was present in all regions with a concentration gradient towards the basal area, starting with the early fixation zone (Fig. 4.3B, ROI 2). Several peaks were assigned to sucrose (*e.g.*, δ = 5.3 ppm), with some overlap with choline (δ = 3.5 ppm) and fructose (δ = 3.8 ppm). In the basal region (region 5), the sucrose peak at δ = 5.3 ppm was hard to distinguish, possibly due to baseline distortions. Overall, the metabolic pattern exhibited in regions 3-4 appeared to be maintained in the basal region (region 5), though attenuated and with a larger linewidth, possibly reflecting a more disorganised structure of the tissue. At the same time active SNF still appeared to take place, indicating this region is not (yet) the senescent zone IV in which the activity would be reduced.

4.3.3 MICROSCOPIC DETECTION OF STARCH CORRELATES WITH MR BASED SUCROSE PROFILE

Starch is a carbohydrate storage polymer that is unique to plants. Indeterminate root nodules are known to form amyloplasts in certain cells, detectable by optical microscopy, especially in the youngest cells of the nitrogen-fixation zone of an actively growing nodule(López *et al.*, 2008). Accumulation of amyloplasts has also been found in cells located behind the division zone in shoot meristems (Jordy, 2004). Zeeman *et al.* speculated that this might be caused by 'a temporary imbalance between carbon import and utilisation as cells move from division to expansion and differentiation' (Zeeman, Kossmann and Smith, 2010). If correct, this marker for high metabolic activity should be reflected in changes to the metabolic profile of bacteroid containing cells. Therefore, I aimed to detect pre- and post-starch granule formation zones in an intact root nodule, and correlate them with sugar metabolites as measured by localised spectroscopy.

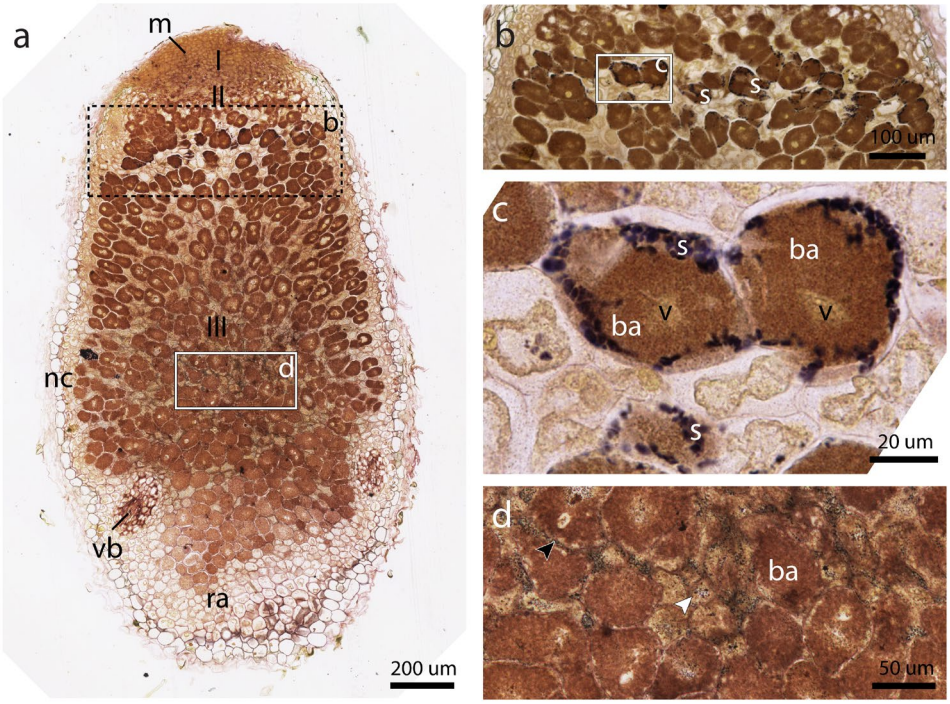

Figure 4.4 Optical microscopy of root nodules reveals multiple starch distribution patterns. Coupes were stained with both Lugol's solution and Toluidine blue. (**A**) A section immediately adjacent to that of Fig. 3A reveals starch distribution throughout the nodule. 10x magnification, scale bar 200 µm. A black dotted rectangle indicates the zone shown in (B) on an alternate section. A white rectangle indicates an enlargement seen in (D). 10x magnification, zoomed; scale bar 50 µm. (**B**) At the first layer of cells in zone III, starch is present as a band (s). A white rectangle indicates the area shown in (C). Alternate section, 20x Magnification, scale bar 100 µm. (**C**) Starch granules (s) are located near the periphery of infected cells. The vacuole (v) reappears in the fixation zone after disorganisation in the infection zone. (B). 40x Magnification, scale bar 20 µm. (**D**) A fine distribution of starch granules can be seen in Zone III contained in nitrogen fixating cells (black arrowhead) and uninfected cells (white arrowhead). Abbreviations: ra, root attachment site; nc, nodule cortex; vb, vascular bundles; m, meristem; s, starch granules; v, vacuole; ba, bacteroids.

Lugol's solution was used to stain amyloplasts (Fig. 4.4A) on an optical section immediately adjacent to that of Fig. 4.3B, to relate the distribution of sucrose and other metabolites to starch. Starch distribution was seen as dark spots, concentrated in a band located in the first layer of the nitrogen fixation zone as well as in smaller amyloplasts throughout the fixation zone (Fig. 4.4B and 4.4D). In the nitrogen fixation zone, amyloplasts were small and dispersed over infected cells (black arrowhead) as well as uninfected interstitial cells (white arrowhead)(Fig. 4.4D). In contrast, the cells present in the first layer on the border of the infection zone (II) and fixation zone (III) exhibited a different distribution of starch (Fig. 4.4B). At higher magnification, large amyloplasts were visible at the periphery of the infected cells, which were almost completely filled with bacteroids (Fig. 4.4C). Thus, sucrose and starch appear to co-localise with SNF

activity. Taken together, starch distribution patterns could provide a possible biomarker for changes in cellular metabolism during nodule development.

4.4 DISCUSSION

This paper showed the feasibility of attaining cellular resolution $7 \times 7 \times 7$ μm^3 in *M. truncatula* root nodules over a relatively large volume $1.8\times 1.4 \times 1.4$ mm^3, opening up new applications for MR microscopy in plant studies (Fig. 4.2A). Individual cells, especially young and mature bacteroids containing cells, were resolved with high contrast, exhibiting a unique 'grey ring' pattern where *S. meliloti* cells accumulated near the cell walls around a central vacuole. Smaller cells, such as present in the meristem, were too small to be resolved individually. The low intensity of the meristem may also reflect a short T_2 relaxation time relative to other structures. Looking towards *in situ* imaging, nodules suffered from lower image contrast and SNR (Fig. 4.2C). A possible reason for the lower image quality may be the abundance of air spaces due to the lack of fixation and vacuum treatment. More quantitative measurements are required to determine the causes of reduced SNR and contrast.

Although the hypo-intense regions caused by small and large air pockets can be detrimental to overall image quality (Supplementary Fig. 4.S2), they also contain useful information. Air pockets in root nodules of *M. truncatula* are of particular interest, because of the delicate balance of oxygen levels required for the proper functioning of the nitrogen fixation. The pockets may thus have a regulatory role, as nitrogenase is paradoxically both dependent on oxygen for carrying out its function but can also be poisoned by oxygen under high concentrations (Lundquist, 2000). Previous MR investigations into root nodules of soybean (*Glycine max*) have focused on investigating the oxygen diffusion barrier, believed to regulate nodule functioning (Brown *et al.*, 1997; Chudek *et al.*, 1997). Furthermore, *Glycine max* root nodules are known to be sensitive to changes in gas perfusion (Macfall *et al.*, 1992). Thus, MRM could be a useful tool to study oxygen regulation mechanisms, due to its ability to detect air spaces through enhanced signal loss.

PRESS localised spectroscopy results show that betaine was distributed throughout the nodule (Fig. 4.3C). The relatively high concentration of betaine could be due to maintaining a high degree of osmoregulation, an indicator of stress, or both (Ashraf and Foolad, 2007). High asparagine levels seen especially in the nitrogen fixation zone indicate significant SNF activity. The presence of asparagine, as well as betaine, was also confirmed by high-resolution 2D correlation spectroscopy on extracts prepared from nodules (Supplementary Fig. 4.S3). Asparagine, together with glutamine, is known to be a major export product of assimilated nitrogen (Sulieman and Tran, 2013). Our results show that asparagine accumulates mostly in active SNF areas (regions 3-5). As such, asparagine was absent in normal root tissue (Supplementary Fig. 4.S5).

Metabolite levels of betaine and asparagine might therefore potentially provide useful markers for stress and SNF activity, respectively. The sucrose concentration gradient,

decreasing from the basal to the apical end of the nodule, may reflect either consumption rates or limitations in transport through the nodule. In conjunction, starch granules appeared to be localised to two specific regions, a band in the transition from infection to fixation zone, and the fixation zone (III) itself (Fig. 4.4). The band seemed to provide support for Zeeman's prediction of amyloplast formation due to a 'temporary metabolic imbalance', though it is located at some distance from the meristem (Fig. 4.4B) (Zeeman, Kossmann and Smith, 2010). As for the fixation zone, it has been observed in the literature that starch amyloplast accumulation in uninfected cells is related to the expression of SNF-related (*nif*) genes (Fig. 4.4D) (Hirsch, Bang and Ausubel, 1983; Hirsch and Smith, 1987). Considering that sucrose was present throughout the nodule, albeit in a diminishing concentration gradient, it is likely that cell-specific metabolism and environmental conditions determine whether and in what quantity starch amyloplasts are formed (Prell and Poole, 2006; Dupont *et al.*, 2012). For instance, sucrose must be metabolised by the host cell in order to provide carboxylic acids that are preferentially taken up by the bacteroids (Yang, Udvardi and Day, 1990; Hohnjec *et al.*, 2007). The observed distribution in size and location of amyloplasts could be affected in this way as well.

As an explorative study of ultra-high field MRM for plant imaging, several recommendations might be of interest to the reader. Sample handling and preparation are essential for high-resolution imaging. More generally, special attention needs to be given to managing sample susceptibility at ultra-high fields, since the inclusion of even small air bubbles in the vicinity of samples can distort image quality significantly, as well as cause line broadening in localised spectroscopic experiments. Another source of sample susceptibility could be the presence of iron in the form of legheamogloblin, which regulates oxygen levels. In bacteroids of mature nodules, up to 25% of the total soluble protein consists of leghaemoglobin (Nap and Bisseling, 1990). The high concentrations of this iron-heme containing protein might have implications for the values of longitudinal relaxation (T_1) and transverse relaxation (T_2) and their interpretation, as these properties may depend strongly on the physiological state of the root nodule when measured. Thus, with further characterisation, susceptibility-weighted imaging may provide a useful method for evaluating the physiological state of root nodules.

Rather than a higher resolution per se, the future applications for MRM at ultrahigh filed for – *in vivo* – imaging are also promising, including longitudinal studies. However, to achieve longitudinal imaging novel coil-insert designs are required with the necessary life support systems. The solenoid coil type used here could be modified to allow for a relatively simple setup that would support whole plants. Vertical-bore MRI systems allow top access to supply light and fresh medium. Additionally, controlled nutrient supply would be desirable, *e.g.* a continuous medium perfusion setup (Flint *et al.*, 2017). Overall, an imaging setup optimised for longitudinal studies would allow testing of stress conditions for host-symbionts, as spectroscopic information can be acquired non-destructively, for example every 30 minutes.

In conclusion, our results demonstrate that MRM at ultra-high fields in conjunction with microcoils provides a promising technique to determine physiology and metabolic profiling non-invasively in plant root nodules. Further research and development on coil design are required to exploit this application to its full potential.

4.5 METHODS

4.5.1 GROWING CONDITIONS *MEDICAGO TRUNCATULA*

Medicago truncatula accession R108 was grown in perlite saturated with Färhaeus medium without nitrate in a growth chamber at a temperature of 21 °C and 16/8 h light/dark cycle (Limpens *et al.*, 2004). Plants were inoculated with *Sinorhizobium meliloti* Rm41 (OD_{600} = 0.1, 2 mL per plant) (Weidner *et al.*, 2013). Root nodules were collected for analysis 21 days after inoculation. Perlite was used as a soil replacement to facilitate the extraction of intact root systems.

4.5.2 SAMPLE PREPARATION

For MRI measurements, a single *M. truncatula* plant was carefully extracted from the perlite substrate. Healthy nodules that exhibited a light-pinkish colour were selected and used for MRI imaging. For *in situ* MRI measurements, a nodule was excised and was directly used for measurements. For *ex vivo* MRI and optical microscopy, root nodules were fixed with paraformaldehyde (4% w/v) and glutaraldehyde (5% v/v) in 50 mM phosphate buffer (pH 7.2) at 4 °C overnight, followed by vacuum treatment for 30 minutes. Samples were then stored at a temperature of 4 °C until use.

Using an SZ40 stereomicroscope (Olympus, Tokyo, Japan), individual nodules were selected that could fit within capillaries with an inner diameter of (1050 ± 50) µm (Hilgenberg GmbH, Malsfeld, Germany). To avoid artefacts during MRI acquisition from air bubbles both within and outside the sample, Perfluorodecalin (PFD) was used to submerge the sample. PFD was chosen because it has several advantageous properties, making it suitable as an infiltration agent. Importantly, it is a non-toxic compound, capable of dissolving both CO_2 and O_2 (Littlejohn and Love, 2012). Furthermore, PFD exhibits a low surface tension (1.9×10^{-2} N m^{-1}), below the limit for stomatal penetration ($2.5\text{-}3.5 \times 10^{-2}$ N m^{-1}) in *Arabidopsis thaliana* leaves (Schönherr and Bukovac, 1972; Littlejohn and Love, 2012), making it useful for reducing air bubbles within the sample without entering the cells. Care was taken to minimise the required amount of PFD as it is known to function as a potent greenhouse gas (Tsai, 2011).

During insertion of the nodule in the centre position of the capillary, both nodule and capillary were kept submerged in PFD. Capillary wax (Hampton Research, California, USA) was then applied to both ends of the open capillary with a MaxWax Pen (Hampton Research, California, USA). Considerable effort was spent on minimising the inclusion of air bubbles within the capillary.

For solution NMR measurements, metabolites were extracted from root and root nodules as described in detail by Kim *et al.* (2010) (Kim, Choi and Verpoorte, 2010). Key

steps included manual excision of root and root nodule tissue and consequent crushing with mortar and pestle in the presence of liquid nitrogen. Samples were then freeze-dried and lastly extracted with an extraction buffer consisting of 50% (v/v) deuterated methanol and 50% D_2O phosphate buffer (pH 6) (Kim, Choi and Verpoorte, 2010).

4.5.3 MRI MEASUREMENTS

A custom solenoid microcoil was built in order to achieve the necessary sensitivity required for high-resolution imaging. For the microcoil assembly, a glass-fibre circuit board was used as a base to hold all the necessary components in place. The radiofrequency (RF) coil consisted of coated 28 AWG (Ø 0.4mm) copper wire, wound into a solenoid with six windings around a glass capillary with an outer diameter of (1500 ± 50) µm. A fixed 1.5 picoFarad (pF) capacitor was placed in series with the RF coil. To complete the resonant circuit, a single 1.5-6 pF variable capacitor was placed parallel to the RF coil and 1.5 pF capacitor, which allowed for fine-tuning the resonant frequency to 950 MHz. The circuit board was then attached to a Micro5 probe (Bruker Biospin, Ettlingen, Germany) compatible circuit holder.

MRI measurements were performed on a Bruker 22.3 T (950 MHz) spectrometer (Bruker Biospin, Ettlingen, Germany), at the uNMR-nl national facility (Utrecht, The Netherlands). The magnet had a vertical bore of 54 mm in diameter and was connected to an Avance III HD console. A Bruker Micro5 probe with exchangeable RF inserts allowed operation of the 1500 µm custom-built solenoid resonator. The Micro5 probe contained a built-in 48 mT m^{-1} A^{-1} (2.88 T m^{-1} at 60 A) triple axial gradient system coupled to GREAT 60 A amplifiers and cooled with a BCU 20 water cooler. Control of spectrometer operations was performed with Paravision 6.0.1 and Topspin 3.1PV running on a CentOS workstation. Sample temperature was maintained at (298 ± 1) K using a BCU II cooler.

High-resolution 3D Fast Low Angle Shot (FLASH) images were acquired with the following parameters: matrix size 256 × 192 × 192; read direction along the largest matrix direction; the field of view was 1.8 × 1.4 × 1.4 mm^3. Resolution 7 × 7 × 7 μm^3 isotropic, number of averages 28, repetition time 120 ms, flip angle 30° and echo time 2.9 ms. Receiver bandwidth was set to 100 kHz. To allow for co-registration with coupes from optical microscopy, the JIVE tool was utilised to generate oblique slices.

A multiple gradient echo (MGE) sequence was also utilised to evaluate the presence of air bubbles and its influence on the image quality. A total of 32 gradient recalled echoes were acquired; initial echo was 2.7 ms, further echoes were spaced 2.8 ms apart resulting in echo times of 2.7, 5.5, 8.3, …, 89.5 ms. Matrix size was 128 × 64 × 64; Read direction along the largest matrix direction; field of view was (1.8×1.4) mm^2. Slice thickness was 1.4 mm; resolution 19 × 19 × 19 μm^3. Number of averages was 24. Repetition time was 120 ms; flip angle 5°.

4.5.3.1 LOCALISED SPECTROSCOPY

Point Resolved Spectroscopy (PRESS) was used for localised magnetic resonance spectroscopy (MRS) on root nodules (Bottomley, 1984, 1987). PRESS employs 90°-180°-

180° orthogonal pulses with concurrent slice selective gradients. The PRESS sequence was preceded by a VAPOR (Variable Pulse Power and Optimized Relaxation Delays) sequence for global water suppression, which consists of seven variable power RF pulses with an optimised relaxation delay (Tkác *et al.*, 1999). Appropriate volumes of interest (voxel) for PRESS were selected from reference FLASH images. Correct positioning of the voxel was also verified afterwards by high-resolution FLASH. Five individual MRS voxel (200x350x350 μm^3) were localised covering various zones in the nodule. The local field homogeneity was optimised over the voxel by MAPSHIM. The field homogeneity was further improved by manual shimming of up to second order shims (Z-Z^2-Z-X-Y-Z-Z^2-Z-XY-XZ-YZ-Z). The field homogeneity resulted in a water line width of 10 Hz. For PRESS measurement, repetition time was set to 1000 ms, echo time was 7.2 ms, and 2048 averages were acquired for a total acquisition time of 34 m 8 s. Spectra were manually phased and automatically baseline corrected with a 3rd or 6th order Bernstein-polynomial fit. Chemical shift alignment was adjusted to the largest peak (3.3 ppm).

4.5.3.2 CHEMICAL SHIFT IMAGING

Chemical Shift Imaging (CSI) was used to acquire a multi-voxel spatial map of metabolic distribution. A large volume of interest was selected using a PRESS approach, consisting of three mutually orthogonal slice selective pulses. Then phase encoding occurred in two directions by applying incremental pulse gradients in each direction, resulting in a matrix of spectroscopic spin echoes.

The following basic parameters were used: Repetition time = 760 ms; echo time = 3 ms; Matrix = 24 × 16; FOV = 1.8 × 1.2 mm^2; slice thickness = 400 µm; resolution = 150 × 150 × 400 μm^3; number of averages = 1024. Spectra were acquired with 2048 points; dwell time 26.4 µs; spectral width 19.93 ppm (18,939 Hz). Magnetic field homogeneity in the selected volume was optimized by shimming the water resonance. A VAPOR suppression scheme was applied for efficient water signal saturation before CSI acquisition.

Reference FLASH images were acquired with the following parameters: matrix size was 96×64; Read direction along the largest matrix direction; field of view was 1.8 × 1.2 mm^2. Slice thickness was 0.1 mm; resolution 19 × 19 × 100 μm^3 isotropic. Number of slices 4; number of averages 128; acquisition time 28 m 40 s. Repetition time was 210 ms; flip angle 30° and echo time 3.26 ms. Receiver bandwidth was set to 50 kHz.

For the processing of the CSI data, the integration of selected signal of specific metabolite areas in magnitude mode was overlaid on reference FLASH images using the Bruker CSI Visualisation Tool.

4.5.4 NMR MEASUREMENTS

NMR measurements were performed on a Bruker 20.0 T (850 MHz) spectrometer with a vertical bore 54 mm in diameter connected to an Avance III HD console. A triple-tuned broadband cryoprobe was used. Topspin 3.2 was used to control the spectrometer and for processing of the acquired data. The sample temperature was maintained at 298K.

^{1}H NMR spectra were collected using a zgpr30 sequence with pre-saturation to suppress water efficiently. Data was acquired into 65k points; dwell time 29.3 µs, spectral width 20 ppm or 17,045 Hz; number of averages, 512; dummy scans 4; pre-scan delay 10 µs. 2D homonuclear ^{1}H-^{1}H experiments were performed using chemical shift correlated spectroscopic sequence (COSY). The following parameters were used: 3400 points in the direct dimension, 400 points in the indirect dimension in Digital Quadrature Mode. Both dimensions zero-filled to 4096 points. Number of averages, 96; dummy scans, 16; Spectral width 12.0 ppm, 10,000 Hz; Temperature 298K.

Assignments were cross-checked against metabolite databases and fitting was performed using Chenomx deconvolution software (Chenomx, Edmonton, Canada)(Cui *et al.*, 2008; Wishart *et al.*, 2009). 1D reference spectra were acquired with parameters as follows: data was acquired into 65k points; dwell time 41.6 µs, spectral width 20 ppm or 12,019 Hz; number of averages, 64; dummy scans 4; pre-scan delay 10 µs. COSY reference spectra were acquired with the following parameters: 4096 points in the direct dimension, 256 points in the indirect dimension in Digital Quadrature Mode. Indirect dimension zero-filled to 4096 points. Number of averages, 4; dummy scans, 16; Spectral width 12.3 ppm, 7200 Hz; Temperature 298 K.

All experimental data were acquired and processed using Paravision 6.0.1 (Bruker Biospin, Ettlingen, Germany) and Topspin 3.1 running on Linux. The default bi-cubic interpolation was applied to enhance the details of the image prior to exporting images. Figures were prepared in Adobe Photoshop CC 2019 and Adobe Illustrator CC 2019 (Adobe Systems Incorporated, Mountain View, California, USA). Stacked spectra were produced in MestReNova (MestreLab Research S.L., Santiago de Compostela, Spain).

4.5.5 LIGHT MICROSCOPY

After MR imaging, the sample material was dehydrated in an ethanol series and subsequently embedded in Technovit 7100 resin (Heraeus Kulzer, Hanau, Germany) according to the manufacturer's protocol. Sections (5 µm) were made by using a microtome (Reichert-Jung, Leica Microsystems, Netherlands), stained with 0.05% Toluidine blue O for 1 min and additionally with Lugol's iodine solution for a few seconds (if applicable). Sections were analysed by using a DM5500B microscope equipped with a DFC425C camera (Leica Microsystems, Wetzlar, Germany).

4.6 REFERENCES

Ashraf, M. and Foolad, M. R. (2007) 'Roles of glycine betaine and proline in improving plant abiotic stress resistance', *Environmental and Experimental Botany*, 59(2), pp. 206–216. doi: 10.1016/j.envexpbot.2005.12.006.

Barker, D. G. *et al.* (1990) 'Medicago truncatula, a model plant for studying the molecular genetics of the Rhizobium-legume symbiosis', *Plant Molecular Biology Reporter*, 8(1), pp. 40–49. doi: 10.1007/BF02668879.

Bottomley, P. A. (1984) 'Point resolved spectroscopy (PRESS)', *US patent*, 4(480), p. 228.

Bottomley, P. A. (1987) 'Spatial Localization in NMR Spectroscopy in Vivo', *Annals of the New York Academy of Sciences*, 508(1 Physiological), pp. 333–348. doi: 10.1111/j.1749-6632.1987.tb32915.x.

Brown, S. M. *et al.* (1997) 'Proton density and apoplastic domains within soybean nodules in relation to the oxygen diffusion barrier', *Plant, Cell and Environment*, 20(8), pp. 1019–1029. doi: 10.1111/j.1365-3040.1997.tb00678.x.

Chudek, J. A. *et al.* (1997) 'An application of NMR microimaging to investigate nitrogen fixing root nodules', *Magnetic Resonance Imaging*, 15(3), pp. 361–368. doi: 10.1016/S0730-725X(96)00273-1.

Cui, Q. *et al.* (2008) 'Metabolite identification via the Madison Metabolomics Consortium Database.', *Nature biotechnology*, 26(2), pp. 162–4. doi: 10.1038/nbt0208-162.

Dakora, F. D. and Atkins, C. A. (1991) 'Adaptation of Nodulated Soybean (Glycine max L. Merr.) to Growth in Rhizospheres Containing Nonambient pO2', *PLANT PHYSIOLOGY*, 96(3), pp. 728–736. doi: 10.1104/pp.96.3.728.

Doran, J. W. and Zeiss, M. R. (2000) 'Soil health and sustainability: managing the biotic component of soil quality', *Applied Soil Ecology*, 15, pp. 3–11. doi: 10.1016/S0929-Get.

Dupont, L. *et al.* (2012) 'The Legume Root Nodule: From Symbiotic Nitrogen Fixation to Senescence', in *Senescence*. InTech, p. 64. doi: 10.5772/34438.

van Dusschoten, D. *et al.* (2016) 'Quantitative 3D analysis of plant roots growing in soil using magnetic resonance imaging', *Plant Physiology*, 170(March), p. pp.01388.2015. doi: 10.1104/pp.15.01388.

Flint, J. J. *et al.* (2017) 'Metabolic support of excised, living brain tissues during magnetic resonance microscopy acquisition', *Journal of Visualized Experiments*, 2017(128), pp. 1–10. doi: 10.3791/56282.

Gavrin, A. *et al.* (2014) 'Adjustment of Host Cells for Accommodation of Symbiotic Bacteria: Vacuole Defunctionalization, HOPS Suppression, and TIP1g Retargeting in Medicago', *The Plant Cell*, 26(9), pp. 3809–3822. doi: 10.1105/tpc.114.128736.

van der Graaf, M. (2010) 'In vivo magnetic resonance spectroscopy: basic methodology and clinical applications.', *European biophysics journal : EBJ*, 39(4), pp. 527–40. doi: 10.1007/s00249-009-0517-y.

Hirsch, A. M., Bang, M. and Ausubel, F. M. (1983) 'Ultrastructural analysis of ineffective alfalfa nodules formed by nif::Tn5 mutants of Rhizobium meliloti', *Journal of Bacteriology*, 155(1), pp. 367–380.

Hirsch, A. M. and Smith, C. A. (1987) 'Effects of Rhizobium meliloti nif and fix mutants on alfalfa root nodule development', *Journal of Bacteriology*, 169(3), pp. 1137–1146. doi: 10.1128/jb.169.3.1137-1146.1987.

Hohnjec, N. *et al.* (2007) ' The Medicago truncatula Sucrose Synthase Gene MtSucS1 Is Activated Both in the Infected Region of Root Nodules and in the Cortex of Roots Colonized by Arbuscular Mycorrhizal Fungi ', *Molecular Plant-Microbe Interactions*, 16(10), pp. 903–915. doi: 10.1094/mpmi.2003.16.10.903.

Jordy, M. N. (2004) 'Seasonal variation of organogenetic activity and reserves allocation in the shoot apex of Pinus pinaster ait', *Annals of Botany*, 93(1), pp. 25–37. doi: 10.1093/aob/mch005.

Kim, B. H. *et al.* (2014) 'Role of Rhizobium, a plant growth promoting bacterium, in enhancing algal biomass through mutualistic interaction', *Biomass and Bioenergy*. Elsevier Ltd, 69, pp. 95–105. doi: 10.1016/j.biombioe.2014.07.015.

Kim, H. K., Choi, Y. H. and Verpoorte, R. (2010) 'NMR-based metabolomic analysis of plants.', *Nature protocols*, 5(3), pp. 536–549. doi: 10.1038/nprot.2009.237.

Kunert, K. J. *et al.* (2016) 'Drought Stress Responses in Soybean Roots and Nodules', *Frontiers in Plant Science*, 7(July), pp. 1–7. doi: 10.3389/fpls.2016.01015.

Limpens, E. *et al.* (2004) 'RNA interference in Agrobacterium rhizogenes-transformed roots of Arabidopsis and Medicago truncatula', *Journal of Experimental Botany*, 55(399), pp. 983–992. doi: 10.1093/jxb/erh122.

Littlejohn, G. R. and Love, J. (2012) 'A simple method for imaging Arabidopsis leaves using perfluorodecalin as an infiltrative imaging medium.', *Journal of visualized experiments : JoVE*, 2(59), pp. 3–6. doi: 10.3791/3394.

López, M. *et al.* (2008) 'Growth and nitrogen fixation in Lotus japonicus and Medicago truncatula under NaCl stress: Nodule carbon metabolism', *Journal of Plant Physiology*, 165(6), pp. 641–650. doi: 10.1016/j.jplph.2007.05.009.

López, M., Tejera, N. A. and Lluch, C. (2009) 'Validamycin A improves the response of Medicago truncatula plants to salt stress by inducing trehalose accumulation in the root nodules', *Journal of Plant Physiology*, 166(11), pp. 1218–1222. doi: 10.1016/j.jplph.2008.12.011.

Lundquist, P. O. (2000) 'Nitrogenase activity in Alnus incana root nodules. Responses to O(2) and short-term N(2) deprivation.', *Plant Physiology*, 122(February), pp. 553–562. doi: 10.1104/pp.122.2.553.

Macfall, J. S. *et al.* (1992) 'Observation of the Oxygen Diffusion Barrier in Soybean (Glycine Max) Nodules with Magnetic-Resonance Microscopy', *Plant Physiology*, 100, pp. 1691–1697.

Metzner, R. *et al.* (2014) 'Belowground plant development measured with magnetic resonance imaging (MRI): exploiting the potential for non-invasive trait quantification using sugar beet as a proxy.', *Frontiers in plant science*, 5(September), p. 469. doi: 10.3389/fpls.2014.00469.

Nap, J. P. and Bisseling, T. (1990) 'Developmental biology of a plant-prokaryote symbiosis: The legume root nodule', *Science*, pp. 948–954. doi: 10.1126/science.250.4983.948.

O'Brien, T. P., Feder, N. and McCully, M. E. (1964) 'Polychromatic staining of plant cell walls by toluidine blue O', *Protoplasma*, 59(2), pp. 368–373. doi: 10.1007/BF01248568.

Ogden, A. J. *et al.* (2017) 'Integrated analysis of zone-specific protein and metabolite profiles within nitrogen-fixing Medicago truncatula-Sinorhizobium medicae nodules', *PLoS ONE*, 12(7), pp. 1–17. doi: 10.1371/journal.pone.0180894.

Pfau, T. *et al.* (2016) 'The intertwined metabolism of Medicago truncatula and its nitrogen fixing symbiont Sinorhizobium meliloti elucidated by genome-scale metabolic models.', *bioRxiv*. doi: 10.1101/067348.

Prell, J. and Poole, P. (2006) 'Metabolic changes of rhizobia in legume nodules', *Trends in Microbiology*, 14(4), pp. 161–168. doi: 10.1016/j.tim.2006.02.005.

Schmittgen, S. *et al.* (2015) 'Magnetic resonance imaging of sugar beet taproots in soil reveals growth reduction and morphological changes during foliar Cercospora beticola infestation', *Journal of Experimental Botany*, 66(18), pp. 5543–5553. doi: 10.1093/jxb/erv109.

Schönherr, J. and Bukovac, M. J. (1972) 'Penetration of Stomata by Liquids', *Plant physiology*, 49(5), pp. 813–819.

Smil, V. (2001) 'Nitrogen cycle and world food production', *World Agriculture*, (Smil), pp. 9–13.

Smith, B. E. (2002) 'STRUCTURE: Nitrogenase Reveals Its Inner Secrets', *Science*, 297(5587), pp. 1654–1655. doi: 10.1126/science.1076659.

Smith, L. T. *et al.* (1988) 'Osmotic control of glycine betaine biosynthesis and degradation in Rhizobium meliloti.', *Journal of bacteriology*, 170(7), pp. 3142–9.

Staudinger, C. *et al.* (2016) 'Evidence for a rhizobia-induced drought stress response strategy in Medicago truncatula', *Journal of Proteomics*. The Authors, 136, pp. 202–213. doi: 10.1016/j.jprot.2016.01.006.

Sulieman, S. and Tran, L. S. P. (2013) 'Asparagine: An amide of particular distinction in the regulation of symbiotic nitrogen fixation of legumes', *Critical Reviews in Biotechnology*, 33(3), pp. 309–327. doi: 10.3109/07388551.2012.695770.

Suzaki, T., Yoro, E. and Kawaguchi, M. (2015) *Leguminous Plants: Inventors of Root Nodules to Accommodate Symbiotic Bacteria*, *International Review of Cell and Molecular Biology*. Elsevier Ltd. doi: 10.1016/bs.ircmb.2015.01.004.

Tkác, I. *et al.* (1999) 'In vivo 1H NMR spectroscopy of rat brain at 1 ms echo time.', *Magnetic resonance in medicine : official journal of the Society of Magnetic Resonance in Medicine / Society of Magnetic Resonance in Medicine*, 41(4), pp. 649–56.

Tsai, W. T. (2011) 'Environmental property modelling of perfluorodecalin and its implications for environmental fate and hazards', *Aerosol and Air Quality Research*, 11(7), pp. 903–907. doi: 10.4209/aaqr.2010.12.0106.

Udvardi, M. K. and Day, D. A. (1997) 'Metabolite transport across symbiotic membranes of legume nodules', *Annual Review of Plant Physiology and Plant Molecular Biology*, 48(1), pp. 493–523. doi: 10.1146/annurev.arplant.48.1.493.

Weidner, S. *et al.* (2013) 'Genome Sequence of Sinorhizobium meliloti Rm41', *Genome Announcements*, 1(1), pp. 12–13. doi: 10.1128/genomeA.00013-12.

Wishart, D. S. *et al.* (2009) 'HMDB: a knowledgebase for the human metabolome.', *Nucleic acids research*, 37(Database issue), pp. D603-10. doi: 10.1093/nar/gkn810.

Xiao, T. T. *et al.* (2014) 'Fate map of Medicago truncatula root nodules', *Development*, 141(18), pp. 3517–3528. doi: 10.1242/dev.110775.

Yang, L. O., Udvardi, M. K. and Day, D. A. (1990) 'Planta the peribacteroid membrane of soybean nodules'.

Ye, H. *et al.* (2013) 'MALDI mass spectrometry-assisted molecular imaging of metabolites during nitrogen fixation in the Medicago truncatula-Sinorhizobium meliloti symbiosis', *The Plant Journal*, *75*(1), pp. 130–145. doi: 10.1111/tpj.12191.

Zeeman, S. C., Kossmann, J. and Smith, A. M. (2010) 'Starch: Its Metabolism, Evolution, and Biotechnological Modification in Plants', *Annual Review of Plant Biology*, 61(1), pp. 209–234. doi: 10.1146/annurev-arplant-042809-112301.

4.7 ACKNOWLEDGEMENTS

Experiments at the 950MHz instrument were supported by uNMR-NL, an NWO-funded National Roadmap Large-Scale Facility of the Netherlands (project 184.032.207). R.S. was supported by the BioSolarCells consortium project U2.3. J.R.K. was supported by the NWO-funded graduate school Netherlands' Magnetic Resonance Research School (NMARRS) graduate school [022.005.029]. D.S was supported by China Scholarship Council (201306040120). A.G.W. was partially supported by European Research Grant 670629 NOMA MRI. Klaartje Houben, Marie Renault and Johan van der Zwan are thanked for technical support at the uNMR-NL facility. Further thanks go out to Volker Lehmann, Henny Janssen and Pieter de Waard for help in troubleshooting.

4.8 SUPPLEMENTARY INFORMATION

4.S1 Video High-resolution 3D FLASH video of fixed and vacuum treated root nodule. Sliced along original matrix orientation. Aspect ratio 4:3, video resolution 1036x768 pixels, 25 frames per second. Duration 6.4 s, 160 frames. Scale bar 200 µm.

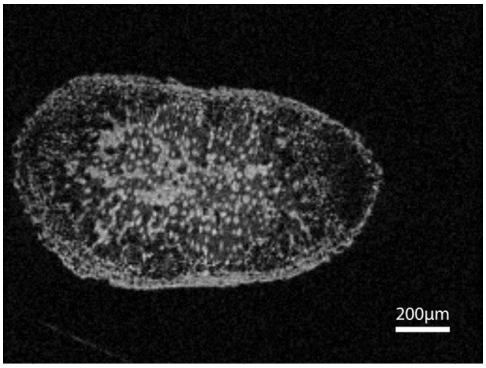

4.S2 Fig. T_2-weighted images reveals susceptibility artefacts caused by air pockets. An MGE sequence was used to acquire scans with 2.7, 5.5, 8.3 ms echo time on a fixed but not vacuum treated nodule, showing a progressive loss of signal as a function of echo time. Nodule Apical-Basal orientation is left-to-right. Dark areas are indicative of air pockets that dephase signal through increased local magnetic susceptibility differences (arrow). Notably, air pockets are variable in size with smaller pockets seen in the basal direction. The meristem and nitrogen fixation area are particularly affected by the signal loss, though the meristem signal loss is likely due to short T_2, not susceptibility. Abbreviations: fx, fixation zone; m, meristem. Scale bar 200 µm.

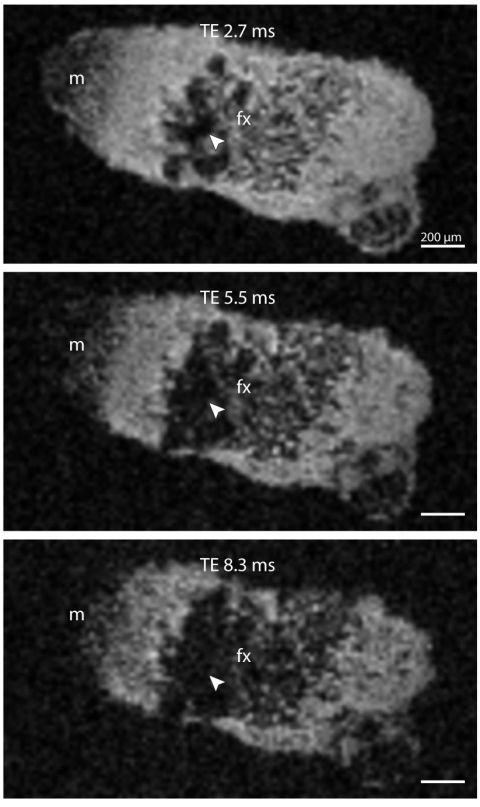

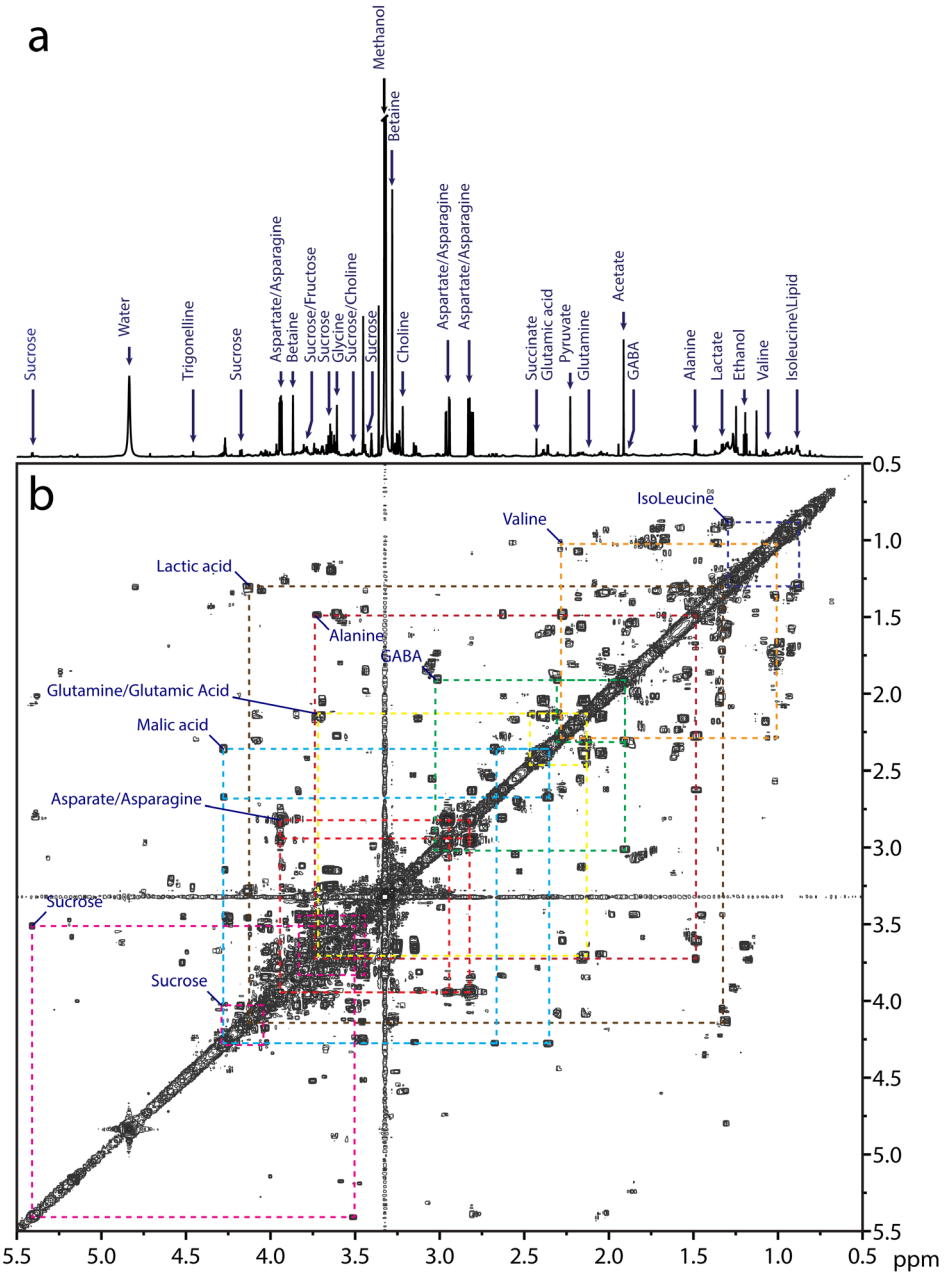

4.S3 Fig. Homo-nuclear ^{1}H correlation spectroscopy (COSY) of root nodule. (**A**) 1D NMR from 0.5 to 5.5 ppm with the most abundant metabolites assigned. Solvent Methanol/D_2O, water suppressed. GABA = γ-aminobutyric acid. (**B**) COSY was used to verify assignments of *in situ* PRESS results. COSY assignments for the most relevant metabolites are indicated with coloured boxes. Range 0.5 to 5.5 ppm, water suppressed.

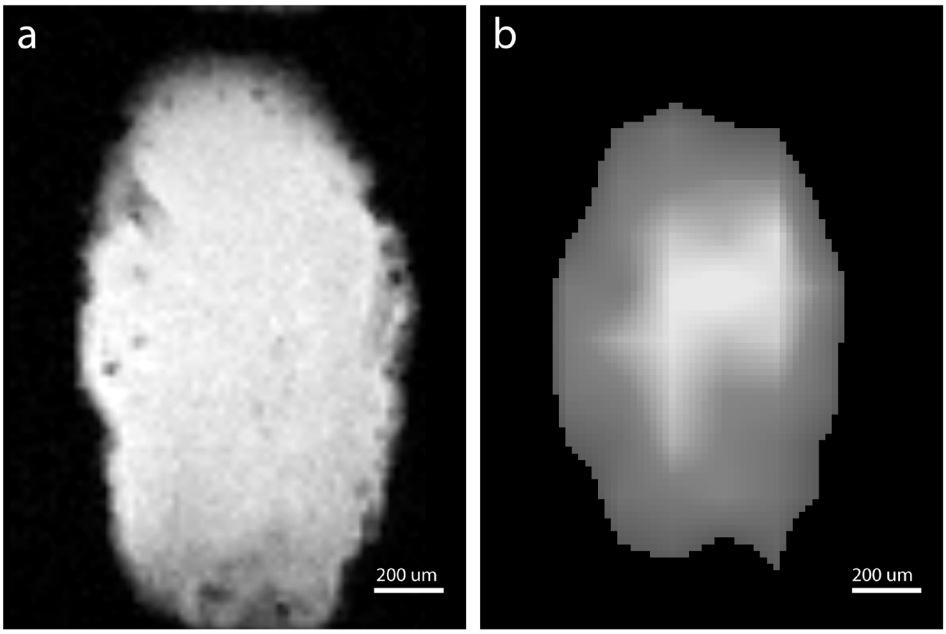

4.S4 Fig. Chemical Shift imaging showing betaine localisation. Nodule Apical-Basal orientation is top to bottom. (**A**) MSME reference image. Note that the CSI volume of interest is larger than the nodule itself. Thus, the distribution of metabolites may be skewed. (**B**) Heat map generated from betaine peak (integration bandwidth 300 Hz).

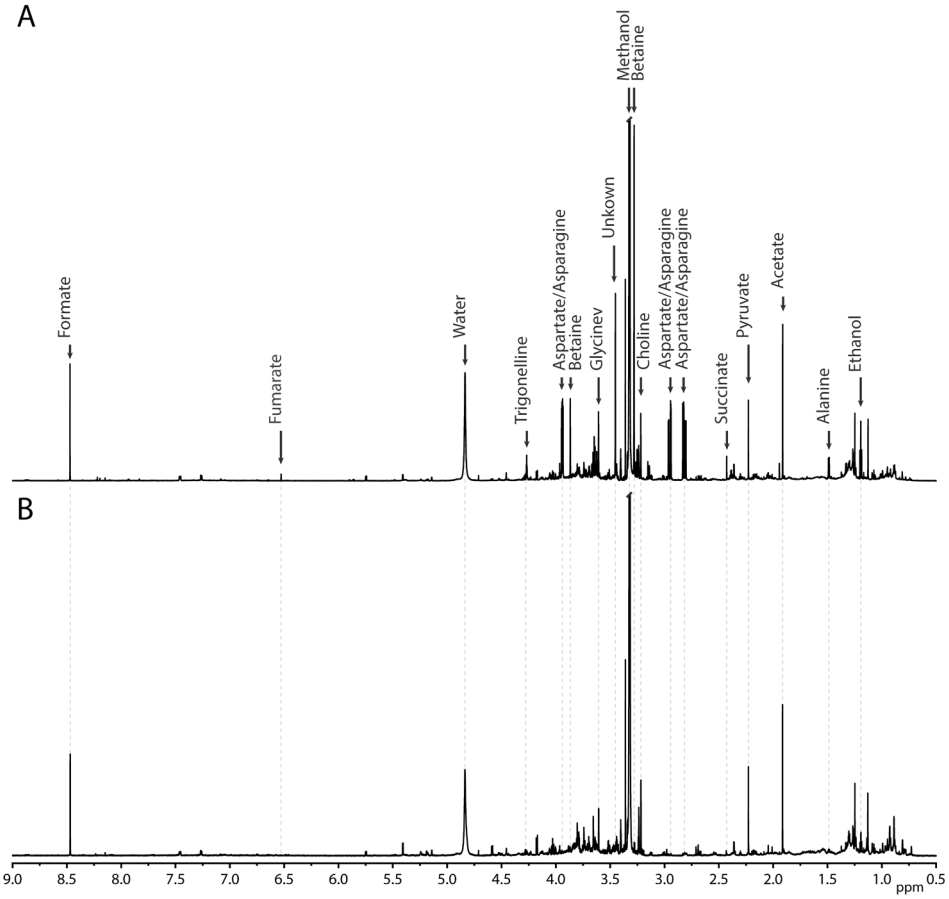

4.S5 Fig. A representative solution state ^{1}H NMR spectrum of root and nodule tissue, revealing differences in several major metabolites. Spectra acquired at 850 MHz. **(A)** Nodule tissue **(B)** Root tissue.

5 GENERAL DISCUSSION AND OUTLOOK

This thesis explored applications of ultra-high field MRI and microcoils to imaging algae and plants. In particular, the unique perspective of MRI in terms of localised spectroscopy and diffusion measurements was brought to the investigation of *Botryococcus braunii*. Furthermore, microcoils were developed, characterised and used to study *Medicago truncatula*.

5.1 OIL LOCALISATION IN *B. BRAUNII* AND BEYOND

The hydrocarbons and oil found in strains of *Botryococcus braunii* strains are a defining feature for the species, as they are implicated in its organisational structure (Weiss *et al.*, 2012; Tanoi, Kawachi and Watanabe, 2014). While there is detailed knowledge of *B. braunii* physiology and anatomy on a cellular level, such information is presently lacking for colony sizes studied here (Suzuki *et al.*, 2013; Uno *et al.*, 2015). In Chapter 2, it was shown that oil localisation is correlated with colony structure, more specifically, colonies exhibiting a hydrocarbon distribution concentrated in two concentric shells. The nature of the two shells and importantly, the causes for their development, warrant further investigation. The distribution of oil in two shells also raises questions on the mobility of oil and water within colonies. Especially the implications for the colony physiology are of interest, since this could relate to growth mechanisms and growth speed.

Two distinct colony types could be distinguished by MR chemical shift (selective) imaging, with the larger type exhibited water channels. Diffusion measurements revealed Apparent Diffusion Coefficient (ADC) values of water linked to the presence of oil and hydrocarbons. However, questions remain concerning the possible development processes through which the two different colony types could have formed. A range of hypotheses is possible, including colony fusion and daughter colony formation. In order to study these hypotheses, longitudinal studies under varying environmental conditions are required to establish the mode of formation and whether these types exist from an early stage or developed at a later stage. MRI would appropriate for such studies as it is highly suited to longitudinal studies of intact, *in-vivo* organisms due to its non-invasive nature (Musse *et al.*, 2009; Van As, Scheenen and Vergeldt, 2009; Van As and van Duynhoven, 2013). Potentially, culturing could even be done within standard NMR tubes, if outfitted with sparging, a light source and regular medium changes.

5.2 DIFFUSION WEIGHTED CHEMICAL SHIFT IMAGING

While in chapter 2, CSSI and CSI were able to localise the oils and hydrocarbons present in *B. braunii*, the presence of water channels raises questions concerning the diffusion of nutrients and oils inside the colonies. Especially the interplay between oil, water and metabolite diffusion is of interest. Since diffusion imaging (DWI) has difficulty distinguishing multiple compounds, as it relies on fitting the combined signal decay, new methodology is required to collect localised information on multiple compounds.

Diffusion Weighted Chemical Shift Imaging (DW-CSI) could potentially satisfy these requirements (Ercan *et al.*, 2015). The DW-CSI sequence is particularly elegant because it combines two of the most attractive capabilities of MRI in a relatively simple manner: localised spectroscopy and diffusion-weighted imaging. While CSI is capable of differentiating multiple molecular species, the addition of a DW module captures information on their respective local diffusive environment, such as vesicle or cell size.

Preliminary results for the DW-CSI have been obtained on a phantom at 17.6T, see Fig. 5.1A. Heatmaps indicate the signal present for a selected resonance, which attenuates as diffusion encoding is increased (Fig. 5.1 B, C, and D).

A series of DW-CSI spectra with increasing diffusion encoding may be stacked in a white-wash plot to visualise the signal decay curves, see Fig. 5.2.

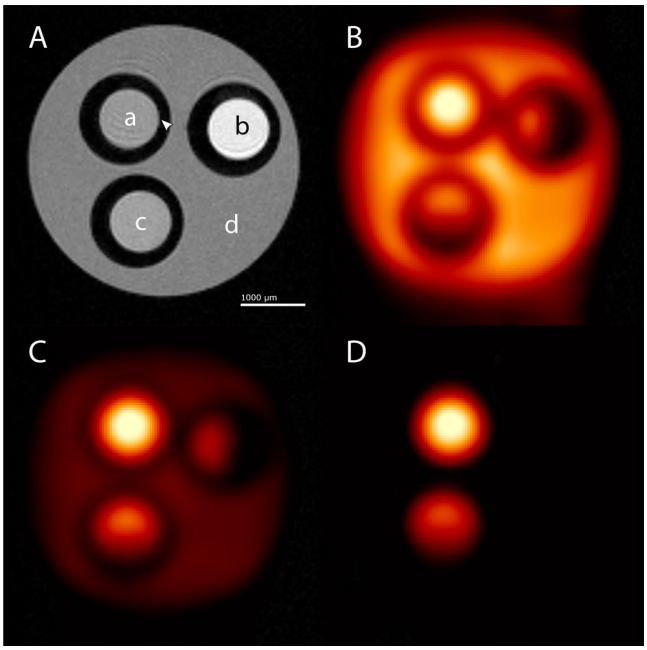

Fig. 5.1 DW-CSI images of reference samples. (A) Reference MSME Image showing three capillaries filled with olive oil (a), hexadecane (b) and oleic acid (c), surround by distilled water (d). Note the chemical shift artefact, caused by the different resonant frequencies of fat/oil relative to water, which displaces the hydrocarbon signal to the right, indicated with a white arrowhead. The artefact is minimised by increasing the receiver bandwidth. (B) Heatmap at minimal gradient strength (54 s mm^{-2}). Some B_0 inhomogeneity is visible in the hexadecane and oleic acid capillaries, possibly caused by susceptibility differences. (C) Heatmap at intermediate gradient strength (740 s mm^{-2}). (D) Heatmap at maximum gradient strength (11,516 s mm^{-2}). Water is fully attenuated at this gradient strength, as well as hexadecane.

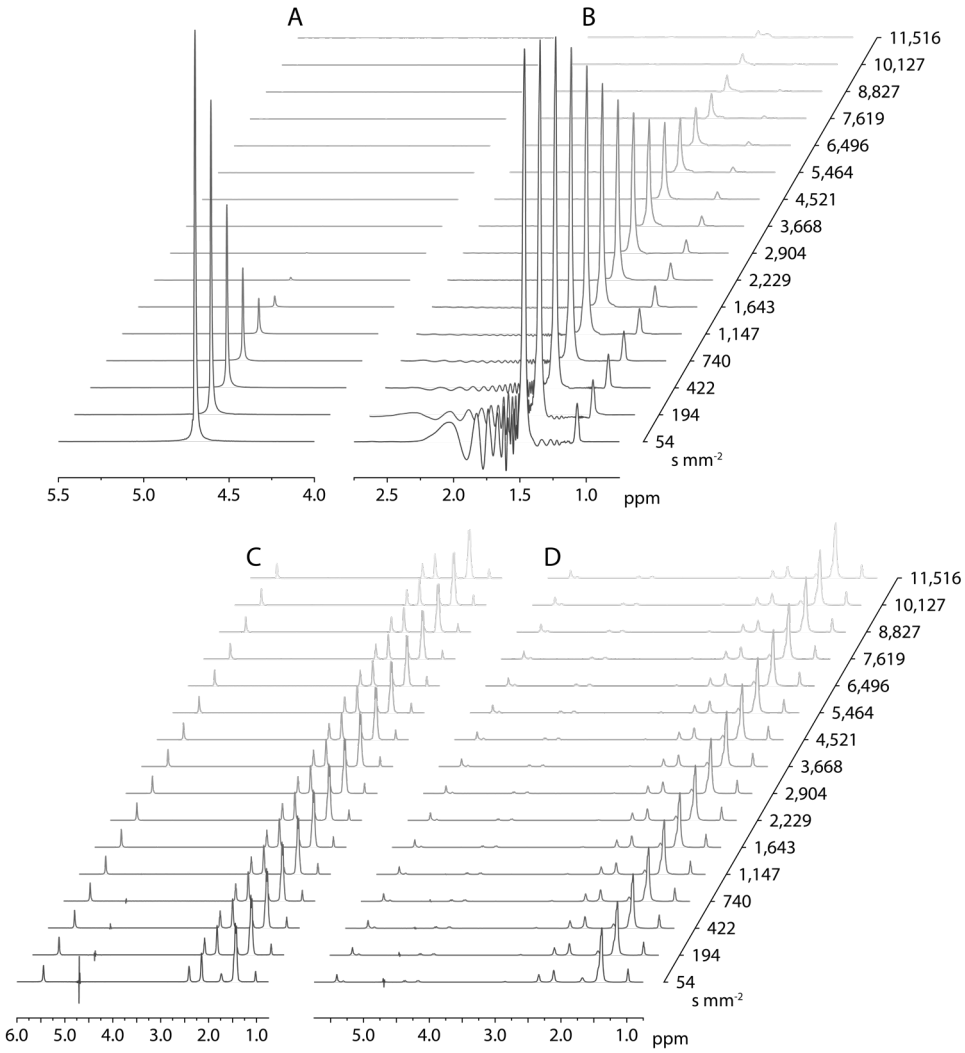

Fig. 5.2 White-washed, stacked plot of DW-CSI reference samples. Each stack depicts a series of representative spectra, with diffusion encoding increasing from front to back. (A) Water spectrum. The resonance at 4.7 ppm is almost completely attenuated at a B-value of 2,904 s mm^{-2}, reflecting the mobile nature of water at 298 K. (B) Hexadecane gives rise to a primary resonance at 1.5 ppm and a side peak at 1.1 ppm. To the left of each peak, eddy currents or stimulated echo artefacts can be seen. The eddy currents are recognised as a distortion of the baseline with an increasing frequency from left to right. These artefacts disappear as the increasing diffusion gradients cause further spoiling. (C) Oleic acid appears resistant to attenuation at the gradient strength used. Around 4.8 ppm, some artefacts due to 50 Hz noise are visible, which is fully attenuated by increased spoiling at around 1,1147 s mm^{-2}. (D) Olive oil presents a similar profile to oleic acid due to it being mainly comprised of triglycerides with oleic acid as a base unit. However, unlike oleic acid, its larger molar mass means it diffuses much slower. Olive oil does not appear significantly attenuated at the gradient strength used.

A

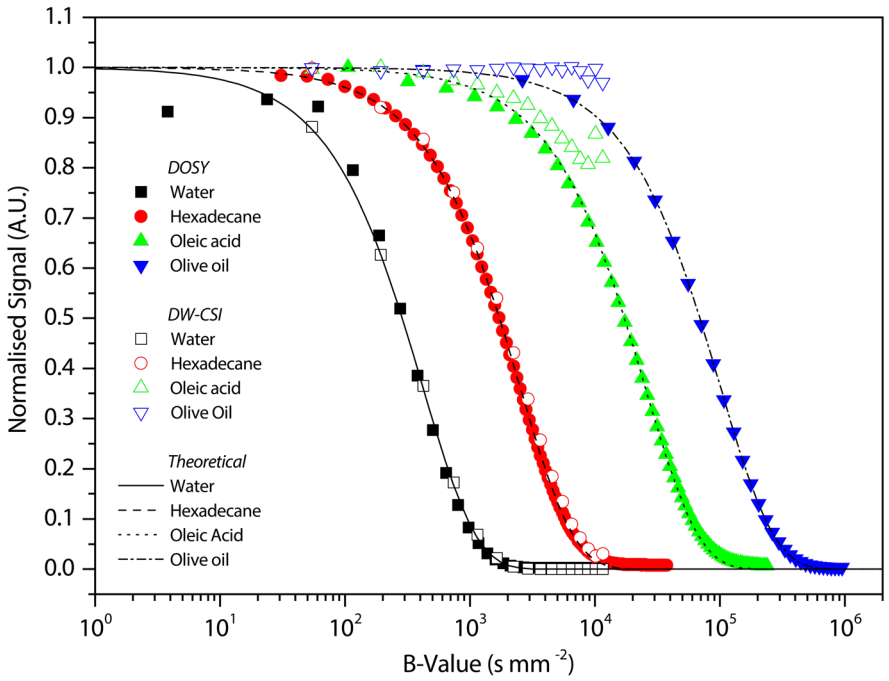

B

Apparent Diffusion Coefficient ($mm^2\ s^{-1}$)		
Compound	DOSY	DW-CSI
Water	$2.42 \cdot 10^{-3} \pm 5.65 \cdot 10^{-5}$	$2.38 \cdot 10^{-3} \pm 6.81 \cdot 10^{-6}$
Hexadecane	$4.04 \cdot 10^{-4} \pm 1.34 \cdot 10^{-6}$	$3.74 \cdot 10^{-4} \pm 3.18 \cdot 10^{-6}$
Oleic acid	$4.03 \cdot 10^{-4} \pm 2.38 \cdot 10^{-7}$	–
Olive oil	$1.01 \cdot 10^{-5} \pm 2.46 \cdot 10^{-8}$	–

Fig. 5.3: (A) Decay curves of reference samples, plotted as normalised signal versus logarithmic (log^{10}) B-value strength. Because of the broad range in molecular weight (M_w) of the reference sample, diffusion encoding strength required for near full attenuation (0.03 relative intensity) differs widely. Up to 800,000 s mm^{-2} is required for olive oil, while 2,000 s mm^{-2} is sufficient for water. DOSY measurements are indicated with closed symbols; DW-CSI results use open symbols. An ideal mono-exponential decay curve is drawn for each sample, based on the ADC calculated for DOSY results. For water and hexadecane, The DW-CSI decay curves correspond well to those of the DOSY measurements. However, for oleic acid and olive oil, the decay curves deviate significantly from the ideal decay curve. As such, no meaningful ADC could be calculated from oleic acid and olive oil DW-CSI data. (B) Resulting ADC values calculated from DW-CSI and NMR DOSY measurements are listed.

The ADC values may then be calculated by mono-exponential fitting of the signal integrals from a series of spectra with increasing B-values (Fig. 5.3A)., Additional NMR DOSY measurements were performed in a separate experiment, to compare the decay

curves from DW-CSI. Ideal decay curves are drawn for the ADC values as determined by DOSY. The calculated ADC values are listed in Fig. 5.3B.

The ADC values for water and hexadecane were found to differ 1.7% and 8.0% respectively, from those measured by DOSY. The standard deviation reflects the closeness of the fit and does not include systematic errors such as possible temperature differences between measurements (Le Bihan *et al.*, 2006). For the higher weight compounds, oleic acid and olive oil, there is an apparent discrepancy between the DOSY and DW-CSI data. Oleic acid is only attenuated by 17.8% compared to the initial signal intensity at a high B-value of 11,516 s mm^{-2}, leading a to a poor fit that does not provide a meaningful ADC value. Likewise, olive oil is not significantly attenuated at the maximum B-value, while DOSY results show clear attenuation. Several factors may contribute to the observed anomalous results, including sample susceptibility differences and eddy currents induced by the gradients.

The current implementation of the DW-CSI sequence does not include eddy current compensation, without which eddy currents can distort or drown out the signal in non-ideal circumstances. An example of this can be seen as line-shape twisting in hexadecane (Fig. 5.2B). Eddy currents can also induce geometric distortions in (DW) images as well over- or underestimation of B-values (Le Bihan *et al.*, 2006). Another cause for the line shape artefact may be a stimulated echo which is caused by unwanted refocussing of residual magnetisation remaining from a previous excitation. Improved phase cycling could reduce the occurrence of such stimulated echoes. Fortuitously, the diffusion encoding gradient in DW-CSI also acts as an additional source of spoiling, reducing stimulated echoes as B-values increase. The extra spoiling causes artefacts to disappear as diffusion encoding increases (Fig. 5.2B).

Olive oil consists of a collection of large compounds (for example, oleic acid triglyceride, 885.43 g mol^{-1}). Its size causes olive oil to require B-values of up to 800,000 s mm^{-2}, in order to be sufficiently attenuated (Fig. 5.3). These high B-value requirements, resulting in long encoding times, could become limiting in samples with high sample susceptibility inhomogeneity. On *in-vivo* samples, this could cause the signal to be dephased before sufficient encoding has taken place. The issue is confounded by the additional time taken up by the diffusion module in a comparatively long CSI sequence. In effect, this currently limits DW-CSI to water or small-molecule diffusion for *in-vivo* measurements on the spectrometer used in this study.

The feasibility of calculating ADC's from DW-CSI measurements has been shown for water and hexadecane. In a separate experiment, 256 mM hexadecane could be detected in 18 m 42 s. Concluding, the DW-CSI sequence is an elegant way of combining information derived from diffusion weighting of secondary metabolites in a spatially resolved manner. However, further research and development, both in sequence and hardware design, is required to utilise this approach to its full potential.

5.3 APPLICATIONS OF SOLENOID MICROCOILS TO PLANTS

In chapter 3, a step-by-step description was provided for testing and characterising solenoid microcoils. The microcoils used in this thesis have a sensitivity up to 4 times that of a 5 mm birdcage resonator (Krug *et al.* 2019, submitted). Given the simplicity and relatively low cost of solenoid microcoils, with excellent performance characteristics, one might expect a wider acceptance of solenoid microcoils by the MRI community than currently seen. In part, this may be facilitated by access to protocols for designing, testing and using microcoils, which this chapter has sought to ameliorate by describing the required knowledge and equipment on a practical level using video. A video publication is especially suited for this purpose due to its inclusive nature, where details are included that authors typically may not consider worthy of description in a written report, and which are nonetheless crucial to successful reproduction of the technology.

Comparing coil performance across different systems is often challenging due to differences in magnetic field strengths, gradient system, consoles, pulse sequences, and choice of parameters, among others. Therefore, the protocol includes a volume-based SNR measure based upon a standardised MSME sequence and sample. In this manner, coils across widely differing systems may be compared, which is facilitated by an initial list of coil SNRs measured across different field strengths (Krug *et al.* 2019, submitted).

The coil demonstrated in the video incorporates a reservoir containing Fomblin as a susceptibility matching fluid. Susceptibility matching is a common strategy for improving microcoil B_1 homogeneity (Olson *et al.*, 1995; Behnia and Webb, 1998; Grant *et al.*, 2001). However, sample induced susceptibility differences, as opposed to those introduced by the coil, become increasingly critical at ultra-high field strengths. The inclusion of microscopic air pockets in roots and microscopic bubbles in capillaries causes fast T_2^* relaxation, with adverse effects on image quality. Vacuum treatment is necessary to achieve distortion-free images at high resolutions. The vacuum treatment yields significant improvement in image quality and SNR compared to non-treated samples, highlighting the importance of sample preparation for MRM.

5.4 CELLULAR RESOLUTION ON *MEDICAGO TRUNCATULA*

In Chapter 4, root nodules of M. truncatula were studied using a home-built solenoid resonator (ID 1.5 mm). Although the high resolution $7 \times 7 \times 7$ μm^3 combined with a relatively large field of view 2.4 x 1.4 x 1.4 mm^3 is useful, the addition of localised spectroscopy makes MRM unique as an investigative tool.

Practical limitations include the long acquisition times for cellular resolutions requiring up to 28 hours, which implies a trade-off between low throughput, high resolutions on single colonies, or lower resolution on multiple samples. Thus, further improvements in sensitivity are desirable, to allow more colonies to be measured in a reasonable time.

The assignments of resonances, especially within the congested carbohydrate region, was confirmed with 2D extraction NMR. In principle, this could also be achieved *in-situ*

with a Localised COSY (LCOSY) or J-resolved sequence (JPRESS). For 2D sequences, the necessary increments in the indirect dimension cause an increase in measurement time, compared to 1D sequences (Ryner, Sorenson and Thomas, 1995; Braakman *et al.*, 2008). Lastly, DW-MRS or DW-CSI could provide information on the localisation of metabolites on a cellular level, *e.g.*, whether metabolites are present within cells or the intracellular space, and overcome the problem of spectral congestion (Kruiskamp *et al.*, 2002; Wang *et al.*, 2017).

The next step for investigating root tissue would be to create a whole-plant life support system, allowing for longitudinal imaging. Several challenges remain, mainly related to the conditions of the root section within the resonator. Currently, liquid PFD is used to match sample susceptibility and remove air bubbles from the sample. For *in-vivo* studies, it would be desirable to avoid submersion of the root, in order to emulate natural root conditions more accurately. Furthermore, PFD evaporates rapidly and is a potent greenhouse gas (Tsai, 2011). Thus, alternative sample treatment and the introduction of life support systems would be needed to perform *in-vivo* imaging. These changes represent a non-trivial challenge to overcome for in-vivo, longitudinal root imaging.

5.5 OUTLOOK

The resolution achievable by MRM continues to improve. However, physical limitations come into play at ultra-high resolution. At imaging resolutions in the range of 10 µm, diffusion attenuation of the signal becomes a limiting factor (Keevil *et al.*, 1998). Diffusion attenuation is illustrated by the resolution dependence of T_2 values recorded by T_2 mapping at 22.3 T (Krug *et al.* 2019, submitted). This limitation is confounded by the exceedingly short T_2^* relaxation rates, in the order of ms, observed in biological samples at high or ultra-high field strengths, *e.g.* 17.6 or 22.3 T. This introduces the need for pulse sequences designed specifically for the challenges of ultra-high field, such as susceptibility differences and the need for accurate measurement of tissue T_2 relaxation. Additionally, high-resolution imaging and DW imaging require strong gradient encoding. Encoding of these gradients needs to be accomplished before the signal has fully relaxed due to T_2 relaxation. Since the sample T_2 limits the gradient durations, the only recourse is to increase the gradient strength. Currently, the commercially available gradients used here reach a maximum gradient strength of 3 T m^{-1} with 60 A gradient amplifiers. Therefore, the most significant performance enhancements possible for MRI at ultra-high field lies in improved gradients, both in terms of resolution and diffusion encoding.

Next, in-vivo studies are likely to become more viable in future research. Continuous flow systems have been demonstrated (Kc *et al.*, 2010), which opens the possibility of growing single colonies in longitudinal studies. Moreover, by varying medium flow rate and composition, different stressing conditions could be investigated. Examples include saline, pH and (micro)nutrient deficiency stresses. The addition of a light source, for example, directed through flexible fibreglass, could also provide the options for controlling irradiation regimes.

Microcoils will continue to be miniaturized with increasingly integrated designs. A promising approach is lab-on-a-chip style flow cells, which incorporate both RF resonator and sample holding cell or flow chamber. A flow chamber built around a cryogenic resonator has also been reported (Koo *et al.*, 2011). Often constructed out of transparent materials, these coils are capable of co-registration with for example optical microscopy. The integration of various approaches to MRM in new coil and gradient designs seems to be the most promising avenue for MRM development.

5.6 ACKNOWLEDGEMENTS

The author would like to thank Karthick B. Sai Sankar Gupta and Fons Lefeber for their capable assistance in the MRI and NMR experiments. Itamar Ronen is thanked for his knowledgeable advice on diffusion and introducing DW-CSI. Further thanks go out to Dieter Gross and Thomas Oerther of Bruker BioSpin GmbH for writing and implementing the DW-CSI pulse sequence for Paravision 5.

5.7 REFERENCES

Van As, H. and van Duynhoven, J. (2013) 'MRI of plants and foods.', *Journal of magnetic resonance (San Diego, Calif. : 1997)*, 229, pp. 25–34. doi: 10.1016/j.jmr.2012.12.019.

Van As, H., Scheenen, T. and Vergeldt, F. J. (2009) 'MRI of intact plants.', *Photosynthesis research*, 102(2–3), pp. 213–22. doi: 10.1007/s11120-009-9486-3.

Behnia, B. and Webb, A. G. (1998) 'Limited-sample NMR using solenoidal microcoils, perfluorocarbon plugs, and capillary spinning', *Analytical Chemistry*, 70(24), pp. 5326–5331. doi: 10.1021/ac9808371.

Le Bihan, D. *et al.* (2006) 'Artifacts and pitfalls in diffusion MRI.', *Journal of magnetic resonance imaging : JMRI*, 24(3), pp. 478–88. doi: 10.1002/jmri.20683.

Braakman, N. *et al.* (2008) 'High resolution localized two-dimensional MR spectroscopy in mouse brain in vivo.', *Magnetic resonance in medicine : official journal of the Society of Magnetic Resonance in Medicine / Society of Magnetic Resonance in Medicine*, 60(2), pp. 449–56. doi: 10.1002/mrm.21662.

Ercan, A. E. *et al.* (2015) 'Diffusion-weighted chemical shift imaging of human brain metabolites at 7T', *Magnetic Resonance in Medicine*, 73(6), pp. 2053–2061. doi: 10.1002/mrm.25346.

Grant, S. C. *et al.* (2001) 'MR microscopy of multicomponent diffusion in single neurons', *Magnetic Resonance in Medicine*, 46, pp. 1107–1112. doi: 10.1002/mrm.1306.

Kc, R. *et al.* (2010) 'Susceptibility-matched plugs for microcoil NMR probes', *Journal of Magnetic Resonance*. Elsevier Inc., 205(1), pp. 63–68. doi: 10.1016/j.jmr.2010.04.001.

Keevil, S. F. *et al.* (1998) 'Reports on Progress in Physics Related content Stray field magnetic resonance imaging'. doi: 10.1016/j.braindev.2014.10.008.

Koo, C. *et al.* (2011) 'A magnetic resonance (MR) microscopy system using a microfluidically cryo-cooled planar coil.', *Lab on a chip*, 11(13), pp. 2197–203. doi: 10.1039/c1lc20056a.

Kruiskamp, M. J. *et al.* (2002) 'Diffusion NMR spectroscopy', *NMR in Biomedicine*, 14(2), pp. 94–111. doi: 10.1002/nbm.686.

Musse, M. *et al.* (2009) 'Monitoring the postharvest ripening of tomato fruit using quantitative MRI and NMR relaxometry', *Postharvest Biology and Technology*, 53(1–2), pp. 22–35. doi: 10.1016/j.postharvbio.2009.02.004.

Olson, D. L. *et al.* (1995) 'High-Resolution Microcoil 1H-NMR for Mass-Limited, Nanoliter-Volume Samples', *Science*, 270(5244), pp. 1967–1970. doi: 10.1126/science.270.5244.1967.

Ryner, L., Sorenson, J. and Thomas, M. (1995) 'Localized 2D J-resolved 1 H MR spectroscopy: Strong coupling effects in vitro and in vivo', *Magnetic Resonance Imaging*, 13(6), pp. 853–869.

Suzuki, R. *et al.* (2013) 'Transformation of lipid bodies related to hydrocarbon accumulation in a green alga, Botryococcus braunii (Race B).', *PloS one*, 8(12), p. e81626. doi: 10.1371/journal.pone.0081626.

Tanoi, T., Kawachi, M. and Watanabe, M. M. (2014) 'Iron and glucose effects on the morphology of Botryococcus braunii with assumption on the colony formation variability', *Journal of Applied Phycology*, 26(1), pp. 1–8. doi: 10.1007/s10811-013-0026-3.

Tsai, W. T. (2011) 'Environmental property modelling of perfluorodecalin and its implications for environmental fate and hazards', *Aerosol and Air Quality Research*, 11(7), pp. 903–907. doi: 10.4209/aaqr.2010.12.0106.

Uno, Y. *et al.* (2015) 'Colony sheath formation is accompanied by shell formation and release in the green alga botryococcus braunii (race B)', *Algal Research*. Elsevier B.V., 8, pp. 214–223. doi: 10.1016/j.algal.2015.02.015.

Wang, A. M. *et al.* (2017) 'Separation and quantification of lactate and lipid at 1.3 ppm by diffusion-weighted magnetic resonance spectroscopy', *Magnetic Resonance in Medicine*, 77(2), pp. 480–489. doi: 10.1002/mrm.26144.

Weiss, T. L. *et al.* (2012) 'Colony organization in the green alga Botryococcus braunii (Race B) is specified by a complex extracellular matrix', *Eukaryotic cell*, 11(12), pp. 1424–40. doi: 10.1128/EC.00184-12.